Stationary Crossflow Breakdown due to Mixed Mode Spectra of Secondary Instabilities

Fei Li,* Meelan M. Choudhari†
NASA Langley Research Center, Hampton, VA, 23681

Lian Duan‡
Missouri University of Science and Technology, Rolla, MO 65409

Numerical simulations are used to study laminar breakdown characteristics associated with stationary crossflow instability in the boundary-layer flow over a subsonic swept-wing configuration. Previous work involving the linear and nonlinear development of individual, fundamental modes of secondary instability waves is extended by considering the role of more complex, yet controlled, spectra of the secondary instability modes. Direct numerical simulations target a mixed mode transition scenario involving the simultaneous presence of Y and Z modes of secondary instability. For the initial amplitudes investigated in this paper, the Y modes are found to play an insignificant role during the onset of transition, in spite of achieving rather large, O(5%), amplitudes of RMS velocity fluctuation prior to transition. Analysis of the numerical simulations shows that this rather surprising finding can be attributed to the fact that the Y modes are concentrated near the top of the crossflow vortex and exert relatively small influence on the Z modes that reside closer to the surface and can lead to transition via nonlinear spreading that does not involve interactions with the Y mode. Finally, secondary instability calculations reveal that subharmonic modes of secondary instability have substantially lower growth rates than those of the fundamental modes, and hence, are less likely to play an important role during the breakdown process involving complex initial spectra.

Nomenclature

A	=	Amplitude of crossflow instability mode or secondary instability mode, measured in terms of peak chordwise velocity perturbation and normalized with respect to freestream velocity
C	=	Wing chord length normal to the leading edge
M	=	Freestream Mach number
m	=	Fourier index of frequency mode
N	=	N factor (i.e., logarithmic amplification ratio) of linear crossflow instability or secondary instability
n	=	Fourier index of spanwise mode
U	=	Base flow streamwise velocity
u	=	Perturbation streamwise velocity
X	=	Chordwise coordinate in the direction perpendicular to the leading edge
Y	=	Cartesian coordinate normal to the X-Z plane
Z	=	Spanwise coordinate, i.e., the coordinate parallel to the wing leading edge
DRE	=	Discrete Roughness Elements
LSIT	=	Linear Secondary Instability Theory
PSE	=	Parabolized Stability Equations
Superscripts		
$+$	=	Wall units
∞	=	Free stream
init	=	Chordwise location where initial amplitudes of perturbations are set

* Aerospace Technologist, Fei.Li@nasa.gov
† Aerospace Technologist, Meelan.M.Choudhari@nasa.gov, Associated Fellow, AIAA
‡ Assistant Professor, duanl@mst.edu, Senior Member, AIAA.

I. Introduction

OVER the years, transition onset correlations based on linear stability theory have been quite successful in predicting trends with respect to changes in aerodynamic design variables and, perhaps more often than expected, have also been found to be reasonable at predicting the actual transition locations.[1] However, wind tunnel[2-4] and flight experiments[5] by Saric and his colleagues have exposed the limitations of linear stability based transition prediction for swept wing boundary layers. By documenting the extended nonlinear development of stationary crossflow vortices ahead of transition and the strong sensitivity of crossflow transition to surface finish and freestream turbulence levels, their experiments have established the need to employ more advanced techniques for transition prediction that account for both receptivity and the nonlinear phase of transition. Transition prediction based on the linear amplification of secondary instabilities[6,7] accounts for the nonlinear evolution of crossflow vortices and, unlike the vortex amplitudes themselves, provides an adequately sensitive measure to predict the onset of transition. Application of this technique to analyzing the flight experiment by Carpenter et al.[5] is described by Li et al.[7] Despite having a stronger physical basis, the secondary N-factor criteria has its own shortcomings. Besides the need to model the initial amplitudes of the primary crossflow vortices, the presence of multiple unstable modes introduces an extra layer of uncertainty in the transition prediction process. Furthermore, while the secondary N-factor predictions may be correlated with the onset of transition, they do not provide any information about the rise of skin friction across the transition zone and its effect on the overall drag. A better understanding of the nonlinear breakdown mechanisms is necessary to help guide the models for the transition zone. Furthermore, knowledge of the breakdown dynamics is also expected to provide potentially valuable insights for the development of transition control techqniques.

There is a considerable body of knowledge concerning the details of the transition process in two-dimensional boundary layers. However, only a few studies related to the laminar breakdown region of transition in crossflow dominated flows have been carried out to date. In recent work, Duan et al.[8] and Choudhari et al.[9] have described the nonlinear breakdown of stationary crossflow vortices via Y and Z modes of secondary instability, respectively. The present work is motivated by the need to extend those results to more complex (and yet controlled) initial spectra to provide the foundation to understanding the breakdown process in the natural disturbance environment involving broadband and stochastic unsteady disturbances. An outline of the flow configuration of interest and the various numerical codes used during the present work is provided in Section II. The previous work involving this flow configuration focused exclusively on the fundamental modes of secondary instability, which have the same spanwise wavelength as the primary crossflow vortices. A brief summary of the mode shapes associated with the fundamental modes and the corresponding breakdown mechanisms is given in Section III. Section IV describes the results of numerical simulations related to the mixed mode transition scenario, which involves a combined evolution of both Y and Z modes of secondary instability. Summary and concluding remarks are provided in Section V. A related accompanying paper[11] extends the prior studies of the same airfoil configuration by investigating the effects of stationary subharmonics of the stationary crossflow vortices that modulate the stationary vortex pattern with a single dominant wavelength.

II. Flow Configuration and Analysis Codes

The flow configuration of interest in this paper is identical to the laminar flow airfoil TAMU-003T-75(v.90) that was previously used by Duan et al.[8] and Choudhari et al.[9] to explore the breakdown characteristics of isolated Y and Z modes, respectively, of the secondary instability of stationary crossflow modes with a specified wavelength. The design process for this laminar flow airfoil was described by Belisle et al.[12] The 9.3 percent thick, 30-degree swept airfoil is designed to achieve natural laminar flow over 60 and 50 percent of the suction and pressure surfaces, respectively, at the design condition of zero degree angle of attack, Mach number of M = 0.75, and chord Reynolds number of approximately 17 million based on freestream speed, a streamwise chord length of 3.658 m (12 ft), freestream temperature of 216.65 K and density of 0.302 kg/m^3. The latter conditions correspond to a flight altitude of 12,192 m (40,000 ft). Design constraints for the wing included a lift coefficient that is typical of subsonic transport aircraft and a wing thickness distribution that is suitable for a mid-size business jet. At the design angle of attack, both Tollmien-Schlichting and crossflow instabilities are sufficiently weak that natural laminar flow should be achievable over a significant portion of the airfoil surface (x/c>0.6 on the suction surface and x/c>0.5 on the pressure side) without any external means of boundary layer control. In this paper, we focus on the off-design condition corresponding to an angle of incidence equal to -1 degree, i.e., the same condition as that used by Li et al.[13] in their PSE and LSIT analysis. At this off-design condition, a stronger crossflow instability exists on the

suction side,[12,13] which provides the basis for potentially implementing DRE-based laminar flow technology at the higher Reynolds numbers of interest.

For the work described in this paper, the mean boundary-layer flow over the suction surface of the airfoil was obtained from the boundary-layer solution obtained by Li et al.[13] It was computed using a boundary layer solver BLSTA,[14] designed specifically for generating accurate boundary layer solutions that are required for boundary layer stability analysis of swept and tapered wings, in conjunction with the inviscid surface-pressure distribution derived from an Euler solution under free flight conditions.[12] The number of wall-normal points used for boundary layer computations was well in excess of that used by Wie[14] for validating the BLSTA code. Sensitivity to streamwise resolution was also assessed by Li et al.[13] by using 115, 229, 457 and 913 points over the chord length of interest (with proportionally greater number of points near the leading edge), and the solution had converged with 115 streamwise points. Similar to the preceding work,[13] the computations presented in this paper are based on 229 points over the chord length. The boundary layer solution computed in this manner is suitably interpolated using cubic splines when necessary.

Linear and nonlinear development of the primary instability (i.e., stationary crossflow vortices) was computed using linear/nonlinear parabolized stability equations (LPSE and NPSE, respectively) as implemented in the Langley Stability and Transition Analysis Codes (LASTRAC).[15] For nonlinear PSE marching, 281 points are used in the wall-normal direction (which is more than sufficient), and the streamwise marching step size was appropriately adjusted for each computation, if necessary, to capture the corresponding modal evolution. We denote the ranges of Fourier modes in the spanwise direction and those in time by *(-m, m)* and *(-n, n)*, respectively. A total of 48 spanwise Fourier harmonics (*m = 48)* is used to compute the nonlinear development of a primary crossflow mode of specified spanwise wavelength, λ; and the truncation error is estimated a posteriori to be at least nine orders of magnitude smaller than the most energetic fundamental mode.

The growth of high-frequency secondary instability modes supported by the finite amplitude stationary crossflow vortex was analyzed by Li et al.[13] with a fully spatial methodology described in an earlier paper.[10] The main difference between the primary and secondary stability analyses is that the basic state for the secondary modes (i.e., the mean boundary layer flow modified by the primary crossflow mode) varies in both surface normal and spanwise directions; and hence, the instability characteristics of the secondary modes must be analyzed using a planar, partial differential equation based eigenvalue problem, rather than the ordinary differential equation based eigenvalue problem of the classical analysis. The selection of grid and other aspects of the numerical solution were based on extensive experience with a similar class of flows and spot checks were made to ensure that the impact of reasonable variations with respect to those choices was negligible. Typically, 121 points in the wall-normal direction and 65 points in the spanwise direction were used for the 2D eigenvalue analysis involving subharmonic modes of secondary instability.

To study the breakdown of finite-amplitude crossflow vortices due to the combined presence of Y and Z modes of secondary instability, a direct numerical simulation (DNS) is performed by solving the Navier-Stokes equations in generalized curvilinear coordinates. The working fluid is assumed to be an ideal gas with linear Newtonian strain-stress relation. The Fourier law is used for the heat flux. A 7^{th}-order weighted essentially non-oscillatory (WENO) scheme[16,17] is used to compute the convective flux terms. This particular WENO scheme combines a high order of accuracy with relatively low dissipation, making it suitable for simulations of compressible transitional flows. The resolution properties of this scheme are documented in many references, e.g., Martin et al.[18] For the viscous flux terms, a 4^{th}-order central difference scheme is used and the 3^{rd}-order low storage Runge-Kutta scheme by Williamson[19] is employed for time integration. Unsteady non-reflecting boundary conditions are imposed at the freestream boundary. At the outflow boundary, a buffer domain technique is used before the primitive variables are extrapolated at the outflow plane. The DNS code has been previously shown to be suitable for computing fully turbulent flows.[20,21] In additional unpublished work, further validation of this code was performed in the context of the propagation of linear instability waves in a 2D, high-speed boundary layer. Convergence studies showed that the 7^{th}-order WENO performs well at a resolution of 10 points per wavelength or higher, depending on the streamwise extent of the computational domain.

The computational domain is approximately aligned with the axis of the primary crossflow mode and extends over more than 100 wavelengths of the Z-mode secondary instability wave with a frequency of 42.5 kHz. For convenience of data processing, the frequency of the Y mode is selected to be 1.5 times the frequency of the Z mode (i.e., 63.75 kHz), which is close to the frequency of the most amplified Y-mode disturbance (62.5 kHz). The size of the computational grid corresponds to $5{,}000 \times 96 \times 307$ points in the chordwise, spanwise, and wall-normal directions, respectively. In terms of wall units of the fully turbulent flow near the outflow of the domain, the grid resolution in the streamwise (X) and spanwise directions (Y) corresponds to $\Delta X^+ \approx 10$ and $\Delta Y^+ \approx 12$, respectively. The first grid point in the wall normal direction is located at $\Delta Z^+ \approx 0.6$. The spanwise resolution is too coarse to

resolve all scales of motion in the latter part of the transition zone as well as the turbulent flow region. However, previous computations[9,10] of the isolated evolution of the Y and Z modes with the same resolution as well as a 2.5 times higher resolution suggest that the limited spanwise resolution is adequate to model the details of the transition process up to and slightly beyond the onset of transition, which is adequate for the purpose of this paper.

III. Fundamental and Subharmonic Modes of Secondary Instability

Li et al.[13] performed NPSE calculations of the nonlinear evolution of isolated stationary crossflow modes for selected values of spanwise wavelength λ and initial amplitude of A_{init} of the crossflow vortex. As discussed by Li et al.,[13] nonlinear effects cause the region of fundamental mode growth to become smaller than the range of unstable locations predicted by linear PSE. Thus, the location of peak disturbance amplitude is further upstream than the downstream branch of the neutral curve based on linear theory. For sufficiently small initial crossflow amplitudes (i.e., relatively smooth airfoil surface), only crossflow modes with spanwise wavelengths near λ = 8 mm achieve large enough amplitudes that are likely to induce a strong secondary instability and, hence, the onset of transition.

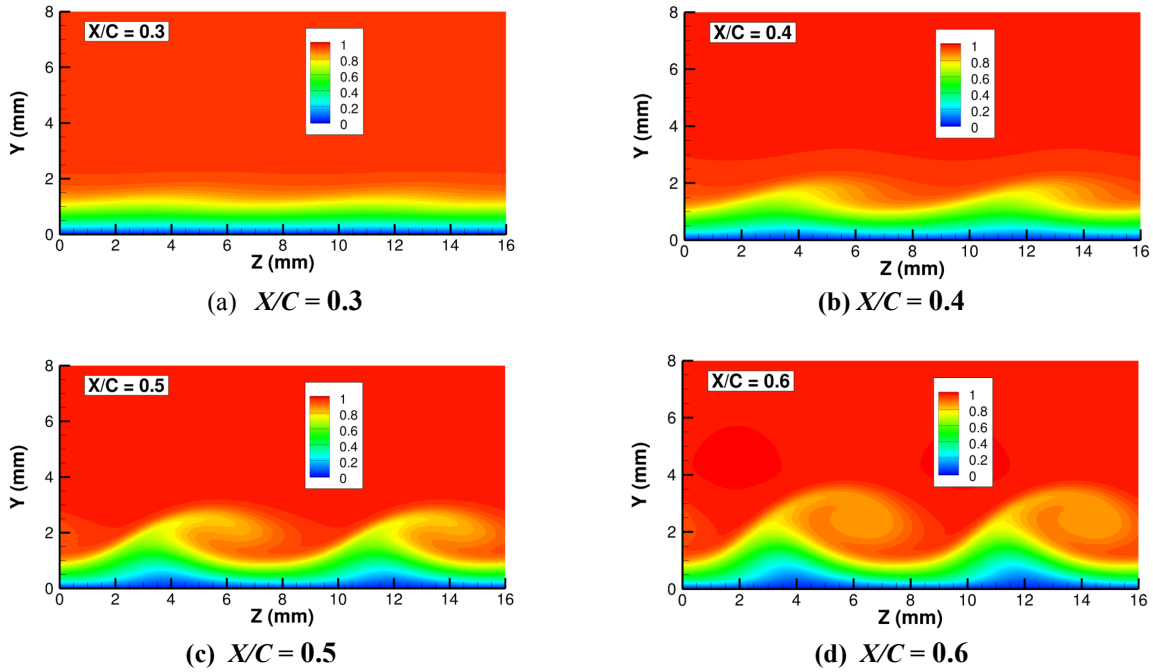

(a) $X/C = 0.3$ (b) $X/C = 0.4$

(c) $X/C = 0.5$ (d) $X/C = 0.6$

Figure 1. Chordwise velocity contours associated with a finite-amplitude crossflow mode.

Figure 1 illustrates the cross-plane velocity contours during the nonlinear evolution of the stationary crossflow mode with λ = 8 mm for the case used for breakdown simulations in Refs. [8 ,9]. The initially undulating contours give way to strongly overturned contours with localized, inclined shear layers that are symptomatic of strongly inflectional velocity profiles in the outer part of the boundary layer. Hence, the appearance of strong shear layers in the outer part of the boundary layer indicates a likely onset of high-frequency secondary instabilities that often signal the onset of laminar breakdown to turbulence. These secondary instability modes can often be classified into two major types:[13] those associated with the strong wall-normal shear of the modified basic state are known as Y modes and those associated with a strong spanwise shear are known as Z modes. At times, when the mean shears in both directions make comparable contributions to the energy production mechanisms associated with the secondary instability, the resulting modes have a mixed character and, hence, are termed as Y/Z modes. In general, the spanwise wavelength of any secondary disturbance can be either equal to that of the fundamental wavelength of the stationary mode or correspond to an integer multiple thereof. The larger wavelength modes are denoted herein as the subharmonic modes of secondary instability.

Illustrative mode shapes depicting the cross-sectional distribution of peak chordwise velocity fluctuation associated with the different secondary mode disturbances are shown in Figs. 2(a) through 2(d). Consistent with the underlying energy transfer mechanisms, the peak fluctuations for the Y modes are concentrated near the top of the inclined shear shear layer associated with the finite amplitude crossflow vortex, precisely where the wall-normal

shear is the highest. On the other hand, the Z-mode fluctuations are concentrated along the lower, inclined portion of the shear layer. These mode shapes also explain the lower phase velocity of the Z modes. The mode shapes of subharmonic disturbances are generally similar to those of the fundamental modes of the same type. However, some subtle differences between the mode shapes of both disturbance types are also apparent from Fig. 2. In particular, the secondary lobes associated with the subharmonic Y modes (which are located below and above the primary shear layer region) are noticeably weaker than those associated with the fundamental modes. In other words, the fluctuations induced by the Y-type subharmonic modes are spatially more concentrated than their fundamental counterparts. An opposite observation may be made for the Z-type subharmonic modes, which extend over a majority of the inclined shear layer. In contrast, the fundamental wavelength modes are more localized in nature. Finally, the peak fluctuations produced by the Z-type subharmonic modes are further away from the surface in comparison to their fundamental counterparts, which is consistent with the higher phase velocity of the subharmonic modes.

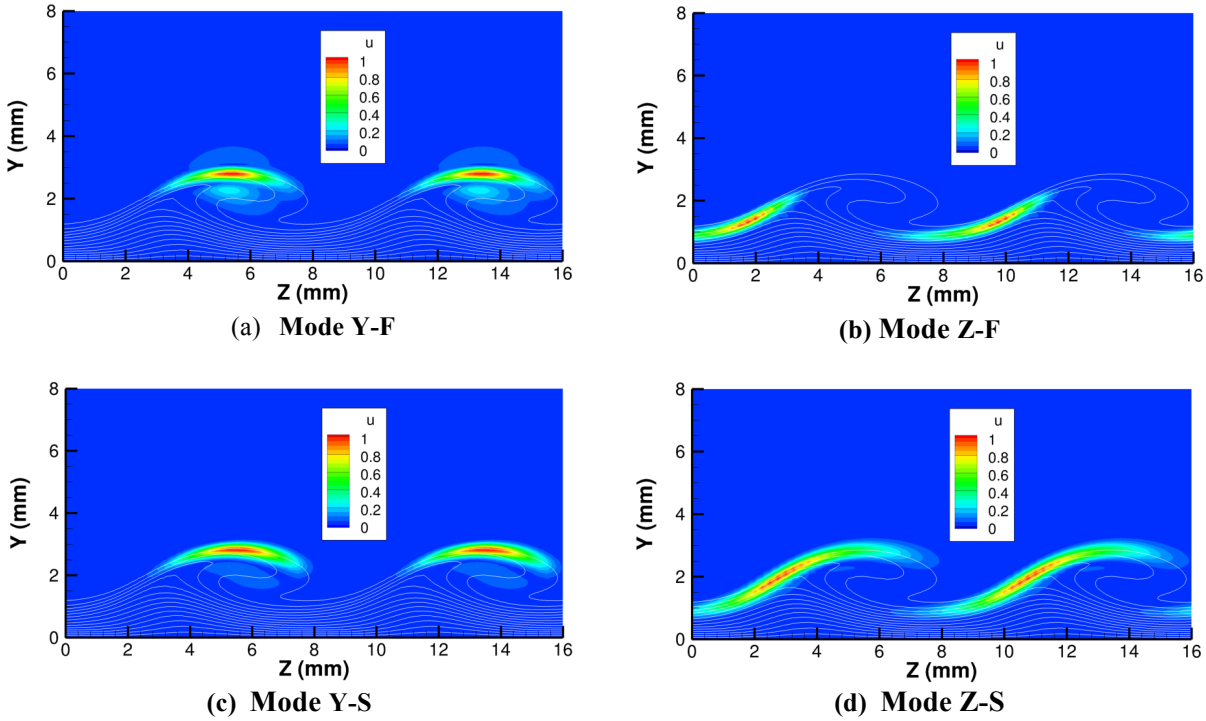

Figure 2. Mode shapes in terms of the magnitude of chordwise velocity fluctuation for four dominant families of secondary instability modes at *X/C* = 0.5. Two spanwise wavelengths of the stationary crossflow vortex with λ = 8 mm are shown in the figure. F: Fundamenal, S: Subharmonic.

Results of secondary instability analysis for the basic state in Fig. 1 have shown that the fundamental mode of the Y type has the highest growth rates in this case. Although not shown herein, the growth rates of subharmonic Y modes are significantly lower than those of the fundamental Y modes, and the same is true for the Z modes as well. In general, the Y-mode secondary disturbances have higher phase velocities than the Z modes. However, the difference between the phase velocities of the two mode types was found to be smaller in the case of the subharmonic modes. Indeed, the phase speeds of fundamental secondary modes appeared to bracket the overall range of phase speeds for the secondary instability modes. In future work, investigations will be carried out to find whether both the growth rates and the phase speed bandwidth of subharmonic modes continue to decrease with increasing subahrmonic wavelengths. Results have also shown that the frequency range of Y modes with fundamental spanwise wavelength is nearly twice as large as the frequency range of the Z modes. While the frequency bandwidth of Y modes appears to decrease from fundamental to subharmonic modes, the frequency range of Z modes appears to shift towards lower values as the spanwise wavelength of the secondary disturbances is increased when going from the fundamental modes to the subharmonic modes.

Because of the substantially lower growth rates of the subharmonic secondary modes, they are less likely to play an important role during the breakdown process, and hence, are not considered further in this paper. However, in principle, the receptivity characteristics of the flow can have a strong influence on which secondary modes would be excited in a given disturbance environment, and we note that the subharmonic secondary modes possess significant growth potential to influence the nonlinear phase of the transition process if the fundamental modes are not excited for some reason. Hence, an understanding of the effects of the subharmonic modes still remains desirable.

IV. Laminar Breakdown due to Combined Evolution of Y and Z Modes of Secondary Instability

Having confirmed that the subharmonic modes are less likely to play an important role during the breakdown of crossflow instability in the flow configuration of interest, the present section targets another canonical aspect of increasing the complexity of inflow disturbances. Specifically, the previous simulations involving the evolution of a single secondary instability mode of the Y type[8] or Z type[9] are extended to address their joint evolution.

The Y and Z modes that achieve the peak N-factors have frequencies of 62.5 kHz and 42.5 kHz, respectively.[13] For the mixed mode transiton analysis, the frequency of the Y mode is adjusted to a slightly higher value of 63.75 kHz so that it is exactly 3/2 times larger than the Z-mode frequency, allowing phase locked nonlinear interactions between the two disturbances via their common harmonic at 127.5 kHz. The growth rate of the Y mode is considerably higher than that of the Z mode. Therefore, the initial amplitudes of the two modes are chosen such that both of them can simultaneously reach large enough amplitudes and collectively influence the location of transition onset.

For computational efficiency, the inflow location for the simulations is chosen to be X/C=0.5, which is well downstream of the respective neutral points (near approximately 45 percent chord location) but is the same location as the inflow location in Refs. [9, 22]. Simulations are performed for various combinations of RMS amplitudes at the inflow location as listed in Table 1, A total of five cases are analyzed, two of which correspond to the earlier simulations involving a single mode inflow disturbance, i.e., Y mode alone[22] and Z mode alone,[9] respectively. The remaining three cases correspond to new simulations of mixed mode evolution wherein the initial amplitude of the Y mode is held fixed at the same level as the purely Y-mode case in Ref. 22. And the inflow amplitude of the Z mode is increased from 0.5 to 1.0 times the value for the Z-mode only case in Ref. 9, such that the highest inflow amplitude of the Z mode in the mixed mode simulations is the same as that in the Z-mode only case. In the order of increasing inflow amplitude of the Z mode, the three mixed mode simulations are denoted in Table 1 as cases Y-Z_{low}, Y-Z_{mid}, and Y-Z_{high}, respectively.

Table 1. Secondary instability initial RMS amplitudes at X/C = 0.5 scaled by the freestream velocity.

Case	Y mode (63.75kHz)	Z mode (42.50kHz)	Z-Y Amplitude Ratio	X_{tr}/C
Y_{only} (Duan et al.[8])	0.00124	0	0	0.551
Y-Z_{low}	0.00124	0.00288	2.33	0.546
Y-Z_{mid}	0.00124	0.00403	3.26	0.543
Y-Z_{high}	0.00124	0.00576	4.65	0.538
Z_{only} (Choudhari et al.[9])	0	0.00576	∞	0.538

An instantaneous snapshot of the DNS flow field in the first mixed mode case (Y-Z_{low}) is presented in Figs. 3 and 4. An isosurface of u = 165 m/s (i.e., approximately 67 percent of the local edge velocity at X/C= 0.54) is shown in Fig. 3, whereas the u = 225 m/s isosurface is plotted in Fig. 4. Upstream of the transition onset location of X/C= 0.546, the u = 165 m/s isosurface in Fig. 3 indicates a series of ridges that are inclined with respect to the vortex axis and are centered along a spanwise location that approximately corresponds to the peak location of the Z-mode secondary instability. The latter location lies between the crest and the trough of axial velocity contours corresponding to the finite amplitude stationary crossflow vortex. The crests and troughs are formed as a result of the momentum exchange induced by the vortex. As nonlinear effects begin to influence the secondary instabilities, the ridges develop a localised spanwise oscillation near the peak of the secondary instability mode shape. Further

downstream, this local deformation begins to spread out, particularly towards the wall and at approximately the same spanwise location relative to the axis of the stationary crossflow vortex. Because the peak of the Z mode of secondary instability was located below the crests of the overturning contours, the tertiary fluctuations can quickly begin to influence the nearwall dynamics, which then leads to the onset of self-sustaining turbulence. On the other hand, the u = 225 m/s isosurface in Fig. 4 clearly depicts the Y-mode instability that is concentrated near the crest of the crossflow vortex and the nonlinear development of this mode resembles that of the varicose instabilities modes of (symmetric) streaks and Goertler vortices in two-dimensional and axisymmetric boundary layers.[23] The flow development in Figs. 3 and 4 confirms that both secondary instability modes seeded at the inflow location achieve large enough amplitudes to undergo nonlinear effects ahead of transition.

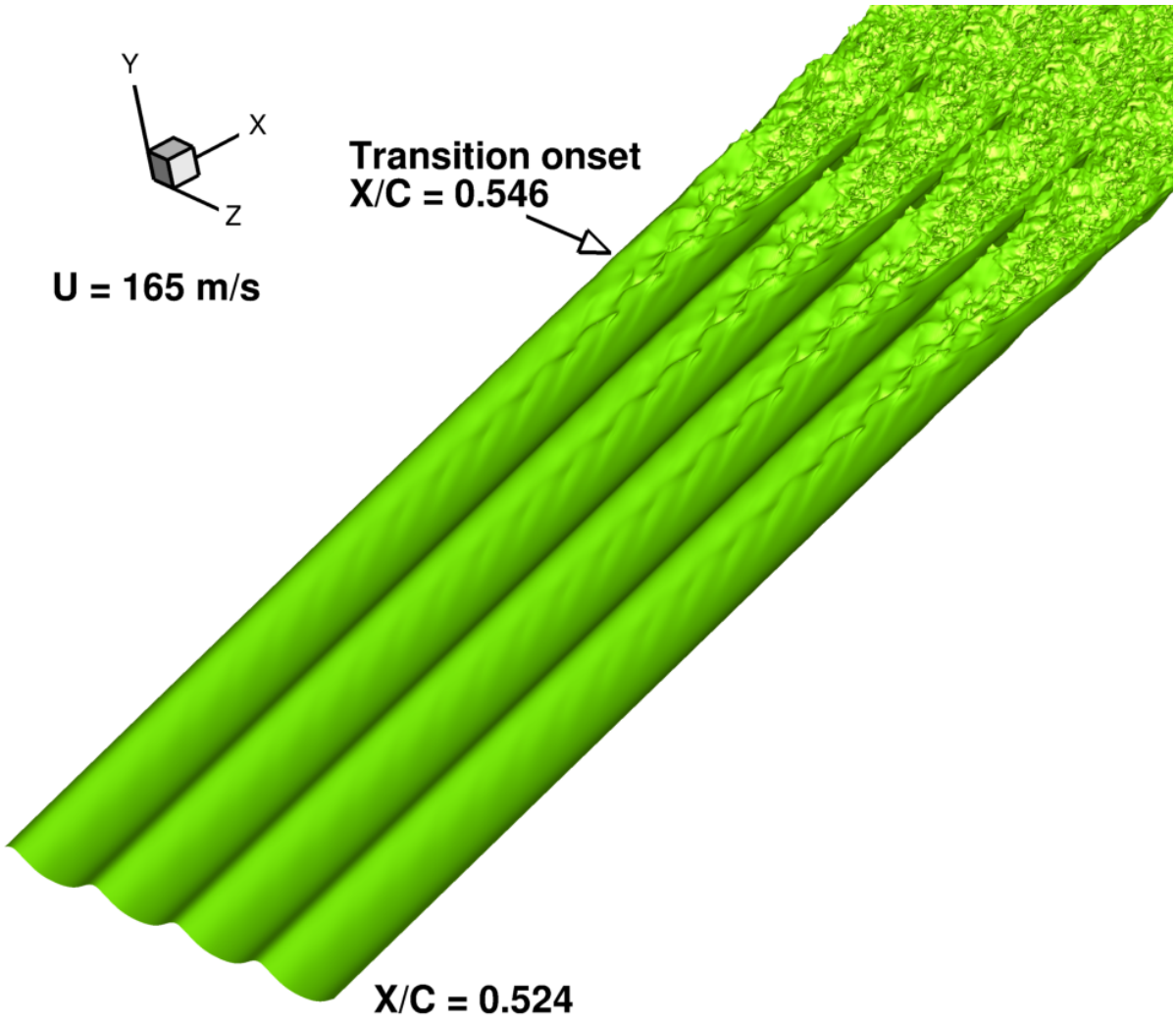

Figure 3. Instantaneous iso-surface corresponding to U = 165 m/s for Case Y-Z_{low}.

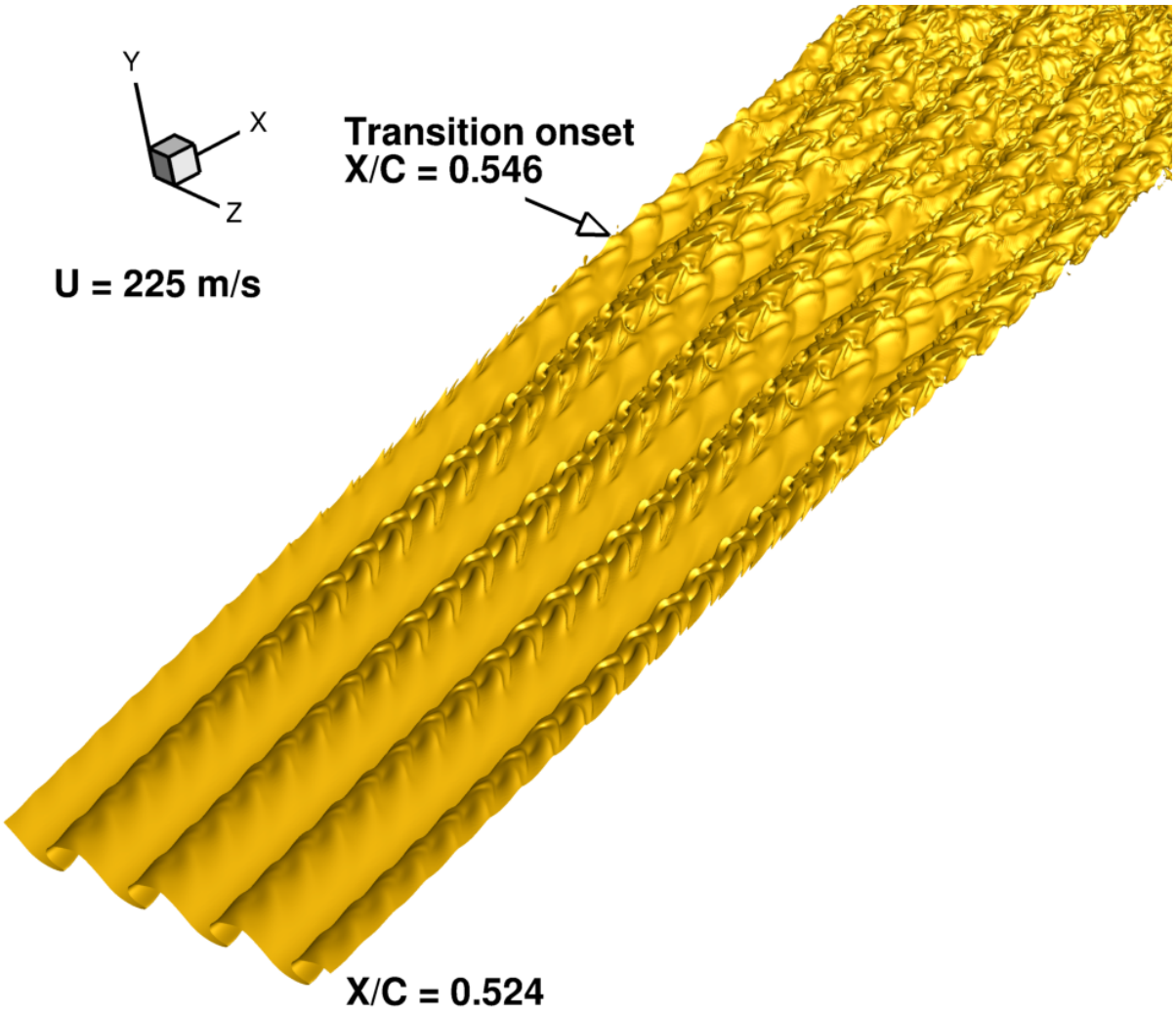

Figure 4. Instantaneous iso-surface corresponding to U = 225 m/s for Case Y-Z_{low}.

Figure 5 shows the time-averaged skin friction contours in the direction of the stationary vortex axis for the lowest amplitude ratio case. The skin friction increases relatively slowly at upstream locations. Then, wedges of much higher skin friction values appear suddenly to spread the turbulence spanwise. Once the wedges originating within individual vortices merge, the flow field become fully turbulent. This transition scenario is identical to that described in Refs. [8, 9] for laminar breakdown due to purely Y-mode and Z-mode fluctuations, respectively. The onset of transition has moved upstream from X/C = 0.551 in the Y_{only} case to $X/C \approx 0.546$, confirming that the addition of Z-mode disturbance at the inflow has contributed to an earlier onset of transition, as expected.

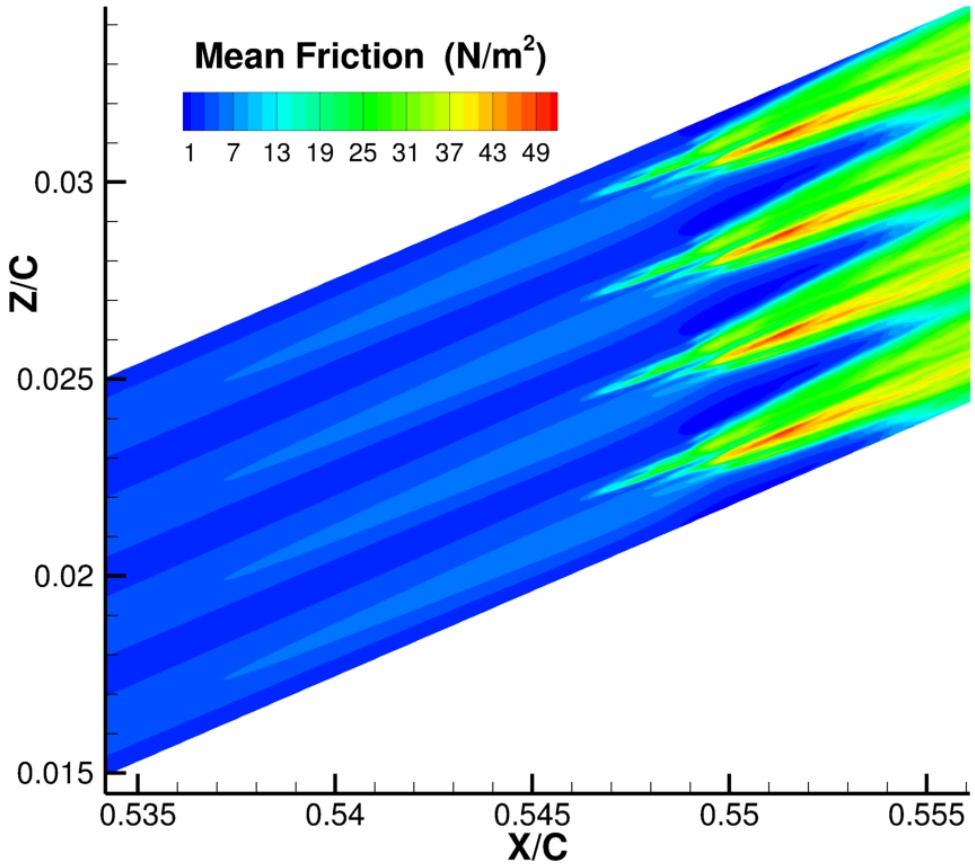

Figure 5. Contours of time averaged skin friction component parallel to vortex axis for the mixed mode case Y-Z_{low} (i.e., lowest non-zero ratio of Z-Y inflow amplitudes).

Figure 6 shows the chordwise evolution of the spanwise averaged skin friction component along the vortex axis for the three mixed mode cases. In each case, a sharp rise in skin friction is clearly identifiable near $X/C = 0.54$. For the discussion in this paper, the transition onset location is associated with the location of skin friction rise. The transition onset locations for the three mixed mode cases are $X/C = 0.546$, 0.543, 0.538, respectively, in the order of increasing initial amplitude of the Z-mode. With the Y-mode amplitude fixed for these cases (Table 1), the upstream movement in transition with increasing Z-mode amplitude confirms the role of Z mode during the transition process.

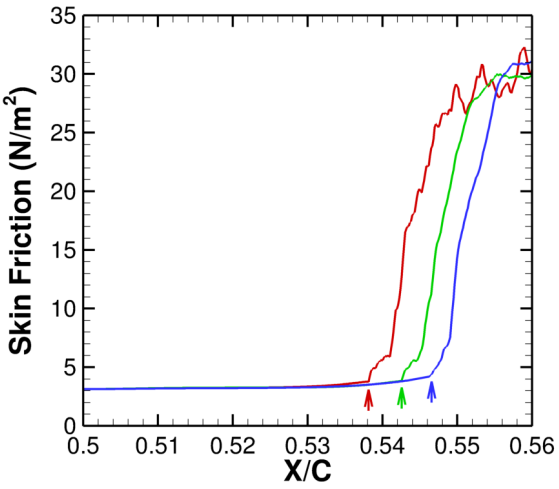

Figure 6. Spanwise averaged skin friction in the direction of vortex axis with arrows indicating transiton onset locations. Blue: Lowest inflow amplitude of Z mode (Y-Z_{low}**), Green: medium Z-mode amplitude (**Y-Z_{mid}**), Red: highest Z-mode amplitude (**Y-Z_{high}**).**

Figure 7 (a) shows the chordwise evolution of the RMS amplitude of secondary disturbances at the fundamental frequency of the Y mode for each of the three mixed mode cases. The accompanying evolution of the Z-mode disturbance with increasing inflow amplitude is shown in Fig. 7(b). Because the inflow amplitude of the Y mode is held fixed in all three cases, the disturbance amplitude at the Y-mode frequency evolves identically in the initial region, until about X/C = 0.54 where the RMS amplitude has reached a value of approximately 5 percent of the freestream velocity. Shortly downstream, however, the Y-mode evolution exhibits a sharp rise that results in more than two-fold increase in the Y-mode amplitude. However, this trend may or may not be physical in view of the limited spanwise resolution in the simulations, which was designed to capture only the initial part of the breakdown process. With increasing inflow amplitude of the Z mode, the rapid rise in Y-mode amplitude moves progressively upstream. However, the rise in Y-mode amplitude always lags the onset of transition as indicated by its position relative to the arrow indicating transition onset. This raises a question regarding the role of Y mode during the transition process.

The evolution of disturbance amplitude at the Z-mode frequency (Fig. 7(b)) indicates a similar trend as the Y-mode evolution described above. Thus, the Z-mode amplitude increases exponentially during the initial, linear phase of development until the growth becomes somewhat slower due to the onset of weakly nonlinear effects. However, after reaching a threshold amplitude of approximately five to six percent, the Z-mode amplitude rises rapidly to its peak value that is nearly three times larger than the threshold amplitude level. The increase in Z-mode amplitude is not as rapid as that of the Y-mode amplitude, but is larger in magnitude, and furthermore, its onset leads the onset of transition in all three cases as compared to the delayed rise in Y-mode amplitude in Fig. 7(a). The increase in Z-mode amplitude continues past the transition onset location, before decreasing eventually as the flow proceeds through the transition region. Again, the results in Fig. 7(b) confirm a significant role of the Z mode during the onset of transition.

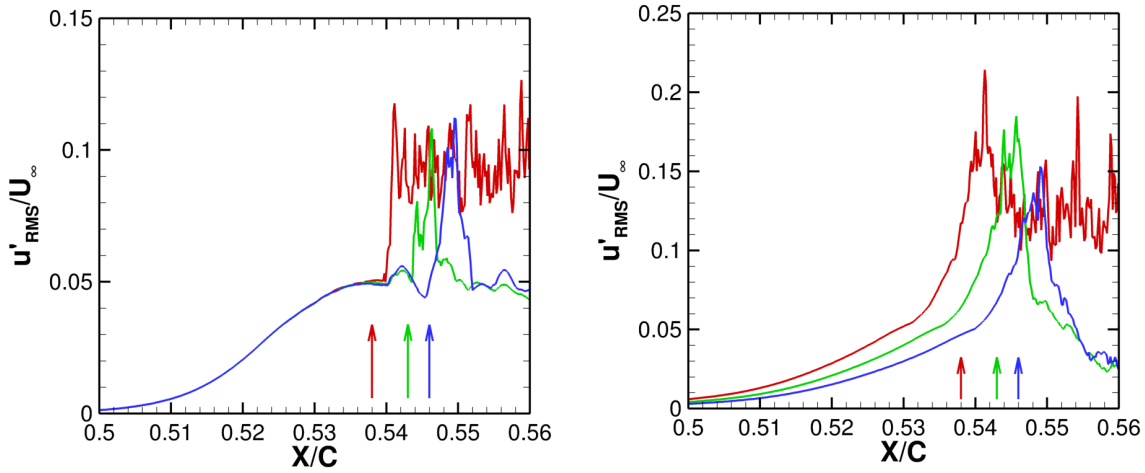

(a) Fundamental harmonic of Y mode, 63.75 kHz **(b) Fundamental harmonic of Z mode, 42.5 kHz**

Figure 7. Comparison of amplitudes for different Z-mode to Y-mode amplitude ratios. Transition locations from Fig. 6 are indicated by the arrows. Curve legends same as Fig. 7.

Figure 8 shows the evolution of disturbance amplitudes at multiple frequencies as determined via Fourier series analysis of the time dependent flow field. As alluded to at the beginning of this section, the Y-mode frequency corresponds to m=3 in the Fourier series, whereas the Z-mode frequency corresponds to *m*=2. Nonlinear self-interactions of the Y-mode generate harmonics m=0, 6, 9, 12, etc., whereas self-interactions of the Z-mode generate m=0, 4, 6, 8, 10, 12, etc. Thus, the Y- and Z-mode disturbances can interact via harmonics 0, 6, 12, and so on. A comparison of amplitude evolution for the mixed mode case with the Y-mode only case is shown in Fig. 8 (a), whereas Fig. 8 (b) shows the comparison of amplitude evolution for the same mixed mode case with the other pure mode case, i.e., the Z-mode only case. Figure 8(a) shows that the presence of the Y mode has no effect on the development of the fundamental Z mode and its first harmonic. Its second harmonic is, however, affected because it is also the first harmonic of the fundamental Y mode. On the other hand, Fig. 8(b) shows that the presence of the Z mode has virtually no effect on the Y mode up to the 4th harmonic of the fundamental Y-mode. Overall, the results in Fig. 8 suggest that the Y-mode and Z-mode fluctuations do not exhibit any significant interactions in spite of achieving rather large amplitudes.

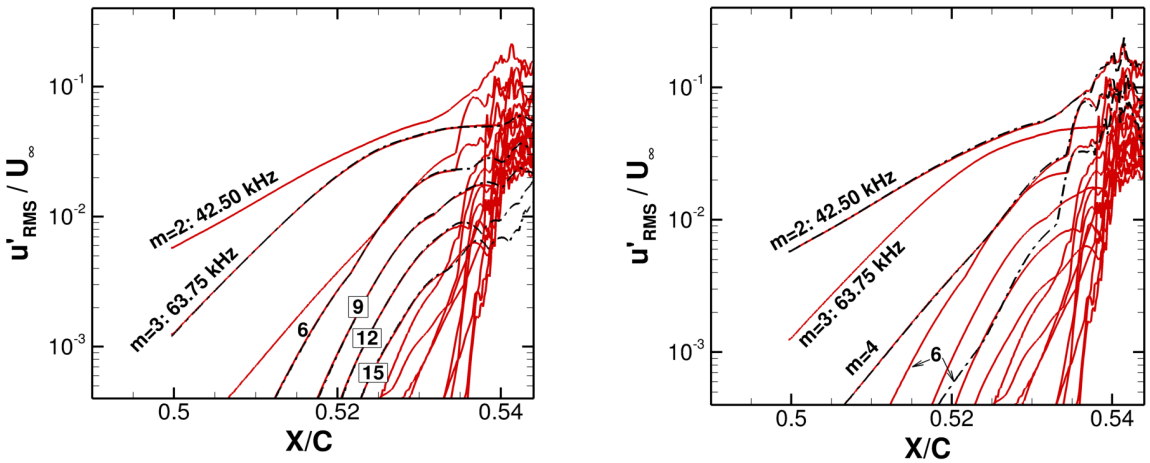

(a) Red lines: Y-Z_{high} mixed mode case, dash-dot black lines: Case Y_{only}. **(b) Red lines: Y-Z_{high} mixed mode case, dash-dot green lines: Case Z_{only}**

Figure 8. Comparison of RMS modal amplitude evolution for mixed mode Case Y-Z_{high} with single mode cases Y_{only} and Z_{only}, respectively.

To further examine the nature of interaction between the Y- and Z-mode fluctuations, the time-RMS contours of fluctuating velocity component along the vortex axis at selected chordwise locations are plotted in Fig. 9. Results for the Y-Z_{low} case are shown in the left column of Fig. 9 whereas contours for the Y-Z_{high} case are shown in the right column. To help interpret the relative magnitudes of the Y- and Z-mode fluctuations regardless of the local value of the disturbance amplitude (which increases more than two orders of magnitude along the length of the computational domain), the fluctuation magnitudes are normalized such that the largest RMS amplitude has a value of unity at each selected station. The time-RMS values are shown as flood contours, and the base flow contours of velocity component along the vortex axis are shown as thin white lines. For each set of inflow disturbance amplitudes, contours are shown at four different locations that represent various stages of secondary instability breakdown. The inflow locations for the Y-Z_{low} and Y-Z_{high} cases are shown in Figs. 9(a) and 9(b), respectively. Here, the fluctuation contours simply denote the Y-mode and Z-mode eigenfunctions with specified amplitudes as listed in Table 1. As explained earlier, the less unstable Z mode has been assigned a larger initial amplitude than the Y mode with the expectation that both of them will reach comparable amplitudes prior to transition onset. The Z modes reside along the inclined boundary of the stationary crossflow vortex, while the Y modes reside on the crest of the vortex. As expected from the relative values of the inflow amplitudes in Table 1, the Z-mode amplitudes are larger than the Y-mode amplitude in both Fig. 9 (a) and Fig. 9 (b).

The second row of Fig. 9 (i.e., sub-figures (c) and (d)) represent the nonlinear stages of the secondary instability breakdown in cases Y-Z_{low} and Y-Z_{high}, respectively. At these locations, the Y and Z modes are clearly distorted from the original mode shapes; but the flow field is still laminar. In the Y-Z_{low} case, the Y-mode amplitude has already become comparable to that of the Z-mode (Fig. 9(c)). On the other hand, in the Y-Z_{high} case (Fig. 9(d)), the larger growth rate of the Y-mode is not sufficient to overcome the increased disparity in inflow amplitudes; and hence, the peak amplitude of Y-mode fluctuations is still smaller than the highest level of Z-mode fluctuations. In both cases, the contours of highest Y-mode fluctuations have expanded considerably from the inflow location, yet they have not begun to merge with the contours associated with highest Z-mode fluctuations. Therefore, little interaction bewteen the two types of modes can be expected at the locations shown in Figs. 9(c)-(d).

The third row of Fig. 9 (Figs. 9(e) and 9(f)) corresponds to the transition onset locations for the respective cases where the skin friction curves begin to rise sharply as indicated in Fig. 6. In both Figs. 9(e) and 9(f), the contours of RMS velocity fluctuation are highly distorted and bear little resemblance to their original shapes in Figs. 9(a) and 9(b). While the Y-mode fluctuations have had a visible impact on the outer part of the vortex structure as depicted in the mean velocity contours, their influence does not appear to have penetrated to the inner region of Z-mode fluctuations. Thus, again, there is no obvious sign of interaction between the two mode types, although the contours originating from the two types of modes appear to have joined at an isolated location. At transition onset, the peak Y-mode amplitudes are seen to be smaller than those of the Z-mode. In addition, the Z-mode contours have spread further inward, getting close to exposing the wall region to high velocity fluctuations, so as to trigger the sharp rise in skin friction just downstream of this location.

The bottom most row in Fig. 9 (i.e., Figs. 9(g) and 9(h)) corresponds to locations that are just downstream of the transiton onset locations for cases Y-Z_{low} and Y-Z_{high}, respectively. At these locations, the Z-mode contours have extended sideways to cover a portion of the vortex span, indicating a spanwise spreading of the laminar breakdown process near the wall. On the other hand, the oscillations originating from the Y-mode are still restricted to regions away from the wall, and hence, does not play a major role in the transition process in spite of achieving rather large peak amplitudes. Because of the different localized regions of the stationary crossflow vortex cross-section in which the Y- and Z-modes of secondary instability are active, the Y mode cannot interact with the Z-mode fluctuations closer to the surface. In all three mixed mode cases, therefore, the Z mode is the one that first reaches the wall and triggers transition to turbulence.

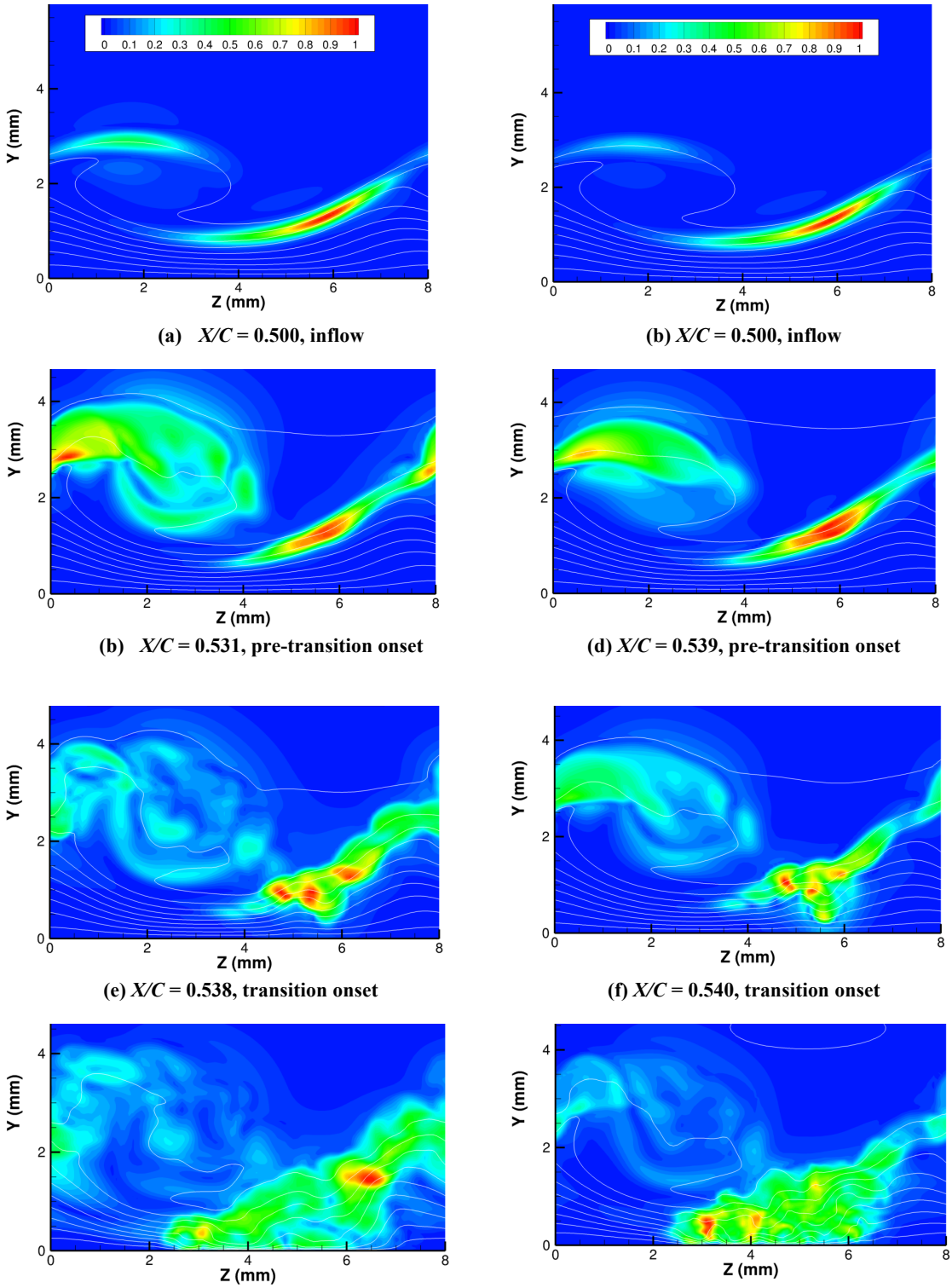

(a) X/C = 0.500, inflow

(b) X/C = 0.500, inflow

(b) X/C = 0.531, pre-transition onset

(d) X/C = 0.539, pre-transition onset

(e) X/C = 0.538, transition onset

(f) X/C = 0.540, transition onset

(g) X/C = 0.542, post transition onset

(g) X/C = 0.541, post transition onset

Figure 9. Vortex-axial time-RMS velocity contours normalized by maximum value in plane. Left column: lowest Z-mode to Y-mode amplitude ratio; Right column: highest.

The results presented in this section indicate that further simulations with additional combinations of inflow amplitudes are necessary to determine the nature of interaction between the Y- and Z-mode fluctuations. Apparently, however, the interaction between Y- and Z-mode fluctuations is unlikely to be observed over a rather narrow range of initial amplitudes, and the isolated breakdown scenarios examined in Refs. 8 and 9 are more likely for an arbitrary combination of inflow amplitudes.

V. Summary

In this paper, previously reported computations of crossflow-induced transition over a realistic swept wing configuration were extended from the evolution of a single, Y or Z type secondary instability mode having the same spanwise wavelength as that of the stationary crossflow vortex to the combined evolution both Y and Z modes with the fundamental wavelength. Specifically, DNS results for selected combinations of initial amplitudes were used to compare the mixed-mode transition simulation with analogous simulations involving each individual mode of secondary instability. For the initial amplitudes investigated in this paper, the Y modes are found to play an insignificant role during the onset of transition in spite of achieving rather large, O(5%), amplitudes of RMS velocity fluctuation prior to transition. Analysis of the numerical simulations shows that this rather surprising finding can be attributed to the fact that the Y modes are concentrated near the top of the crossflow vortex and exert relatively small influence on the Z modes that reside closer to the surface and can lead to transition via nonlinear spreading that does not involve interactions with the Y mode.

The subharmonic secondary modes are found to have lower growth rates as expected, and hence, are deemed relatively unimportant during the breakdown process for the configuration of interest. However, if the receptivity characteristics are such that the initial amplitudes of the fundamental secondary modes are very low, then the subharmonic modes could possibly induce transition on their own because of their relatively significant growth potential to influence the nonlinear phase of the transition process.

Acknowledgments

This work was performed as part of the Revolutionary Computational Aerosciences discipline under the Transformational Tools and Technologies project of NASA's Transformative Aeronautics Concepts Program. The authors would like to thank Prof. Pino Martin of the University of Maryland for providing the original version of the DNS code used in this effort.

References

[1] Bushnell, D., Malik, M. R., and Harvey, W. D., "Transition Prediction in External Flows via Linear Stability Theory," In *Symposium Transsonicum III*, J. Zierep and H. Oertel, Jr., eds., Springer Verlag, Berlin Heidelberg, 1989, pp. 225–242.

[2] Reibert, M.S. and Saric, W.S., "Review of Swept-Wing Transition," AIAA Paper 97-1816, 1997.

[3] White E. B. and Saric W. S., "Secondary Instability of Crossflow Vortices," *J. Fluid Mech*. Vol. 525, 2005, pp. 275–308.

[4] Saric, W. S., Carillo, R. B., and Reibert, M. S., "Leading Edge Roughness as a Transition Control Mechanism," AIAA Paper 98-0781, 1998.

[5] Carpenter, A. L., Saric, W. S., and Reed, H. L., "Laminar Flow Control on a Swept Wing with Distributed Roughness," AIAA Paper 2008-7335, 2008.

[6] Malik, M. R., Li, F., and Chang, C.-L., "Crossflow Disturbances in Three-Dimensional Boundary Layers: Nonlinear Development, Wave Interaction and Secondary Instability," *J. Fluid Mech.,* Vol. 268, 1994, pp. 1–36.

[7] Li, F., Choudhari, M. M., Chang, C.-L. Streett, C. L., and Carpenter, M. H., "Computational Modeling of Roughness-Based Laminar Flow Control on a Subsonic Swept Wing," *AIAA J.,* Vol. 49, No. 3, March 2011, pp. 520–529.

[8] Duan, L., Choudhari, M., and Li, F., "Direct Numerical Simulation of Crossflow-Induced Transition in a Swept Wing Boundary Layer," AIAA Paper 2013-2617, 2013.

[9] Choudhari, M., Li, F., Duan, L., Carpenter, M. H., Streett, C. L. and Malik, M. R., "Towards Bridging the Gap in Hoslistic Transtion Prediction via Numerical Simulations," AIAA Paper 2013-2718, 2013.

[10] Li, F. and Choudhari, M., "Spatially Developing Secondary Instabilities and Attachment Line Instability in Supersonic Boundary Layers," AIAA Paper 2008-590, 2008.

[11] Choudhari, M. M., and Li, F., "Influence of Stationary Crossflow Modulation on Secondary Instability," Submitted to Aviation-2016 Conference, Washington, D.C., 2016.

[12] Belisle, M., Neale, T., Reed, H., and Saric, W., "Design of a Swept-Wing Laminar Flow Control Flight Experiment for Transonic Aircraft," AIAA paper 2010-4381, 2010.

[13] Li, F., Choudhari, M. M., Carpenter, M. H., Malik, M. R., Chang, C.-L., and Streett, C. L., "Roughness Based Crossflow Transition Control for a Swept Airfoil Design Relevant to Subsonic Transports," AIAA Paper 2010-4380, 2010.

[14] Wie, Y.-S., "BLSTA – A Boundary Layer Code for Stability Analysis," NASA CR 4481, 1992.

[15] Chang, C.-L., "Langley Stability and Transition Analysis Code (LASTRAC) Version 1.2 User Manual," NASA/TM-2004-213233, June, 2004.
[16] Jiang, G. S. and Shu, C. W., "Efficient Implementation of Weighted ENO Schemes," *Journal of Computational Physics*, Vol. 126, No. 1, 1996, pp. 202–228.
[17] Taylor, E. M., Wu, M., and Martin, M. P., "Optimization of Nonlinear Error Sources for Weighted Non-Oscillatory Methods in Direct Numerical Simulations of Compressible Turbulence," *Journal of Computational Physics*, Vol. 223, No. 1, 2006, pp. 384–397.
[18] Martin, M. P., Taylor, E. M., Wu, M., and Weirs, V. G., "A Bandwidth-Optimized WENO Scheme for the Effective Direct Numerical Simulation of Compressible Turbulence," *J. Comp. Phys.,* Vol. 220, 2006, pp. 270–289.
[19] Williamson, J., "Low-Storage Runge-Kutta Schemes," *Journal of Computational Physics*, Vol. 35, No. 1, 1980, pp. 48–56.
[20] Duan, L., Beekman, I., and Martin, M. P., "Direct Numerical Simulation of Hypersonic Turbulent Boundary Layers. Part 3: Effect of Mach Number," *Journal of Fluid Mechanics*, Vol. 672, 2011, pp. 245–267.
[21] Duan, L., Choudhari, M., and Wu, M., "Numerical Study of Acoustic Radiation due to a Supersonic Turbulent Boundary Layer," *Journal of Fluid Mechanics,* Vol. 746, 2013, pp. 165–192.
[22] Duan, L., Choudhari, M., and Li, F., "DNS of Laminar-Turbulent Transition in Swept-Wing Boundary Layers," Proceedings of the 2014 Summer Program, Center for Turbulence Research, 2014, pp. 273-283.
[23] Li, F., Choudhari, M. M., Chang, C.-L., Wu, M., and Greene, P. T., "Development and Breakdown of Görtler Vortices in High-Speed Boundary Layers," AIAA Paper 2010-705, 2010.